Article

Impact of ionizing radiation on superconducting qubit coherence

https://doi.org/10.1038/s41586-020-2619-8

Received: 25 January 2020

Accepted: 5 June 2020

Published online: 26 August 2020

Check for updates

Antti P. Vepsäläinen[1]✉, Amir H. Karamlou[1], John L. Orrell[2]✉, Akshunna S. Dogra[1,4], Ben Loer[2], Francisca Vasconcelos[1], David K. Kim[3], Alexander J. Melville[3], Bethany M. Niedzielski[3], Jonilyn L. Yoder[3], Simon Gustavsson[1], Joseph A. Formaggio[1], Brent A. VanDevender[2] & William D. Oliver[1,3]

Technologies that rely on quantum bits (qubits) require long coherence times and high-fidelity operations[1]. Superconducting qubits are one of the leading platforms for achieving these objectives[2,3]. However, the coherence of superconducting qubits is affected by the breaking of Cooper pairs of electrons[4–6]. The experimentally observed density of the broken Cooper pairs, referred to as quasiparticles, is orders of magnitude higher than the value predicted at equilibrium by the Bardeen–Cooper–Schrieffer theory of superconductivity[7–9]. Previous work[10–12] has shown that infrared photons considerably increase the quasiparticle density, yet even in the best-isolated systems, it remains much higher[10] than expected, suggesting that another generation mechanism exists[13]. Here we provide evidence that ionizing radiation from environmental radioactive materials and cosmic rays contributes to this observed difference. The effect of ionizing radiation leads to an elevated quasiparticle density, which we predict would ultimately limit the coherence times of superconducting qubits of the type measured here to milliseconds. We further demonstrate that radiation shielding reduces the flux of ionizing radiation and thereby increases the energy-relaxation time. Albeit a small effect for today's qubits, reducing or mitigating the impact of ionizing radiation will be critical for realizing fault-tolerant superconducting quantum computers.

Over the past 20 years, superconducting qubit coherence times have increased by more than five orders of magnitude due to improvements in device design, fabrication and materials, from less than 1 ns in 1999[14] to more than 100 μs in contemporary devices[15,16]. Nonetheless, to realize the full promise of quantum computing, far longer coherence times will be needed to achieve the operational fidelities required for fault-tolerance[17].

Today, the performance of superconducting qubits is limited in part by quasiparticles—a phenomenon known colloquially as 'quasiparticle poisoning'. Although it was suggested[18] and recently confirmed[19] that high-energy cosmic rays result in bursts of quasiparticles that reduce the quality factor in superconducting granular aluminium resonators, there has been no quantitative model or experimental validation of the effect of environmental ionizing radiation on superconducting qubits.

Here we measure the impact of environmental radiation on superconducting qubit performance. We develop a model and determine its parameters by measuring the effect of radiation from a calibrated radioactive source on the qubit energy-relaxation rate. We use this model to infer the energy-relaxation rate $\Gamma_1 \approx 1/4\ \mathrm{ms}^{-1}$ for our qubit if it were limited solely by the measured level of naturally occurring cosmic rays and background environmental radiation present in our laboratory. We then demonstrate that the deleterious effects of this external radiation can be reduced by protecting the device with a lead shield. The improvement in qubit energy-relaxation time from this independent shielding measurement is consistent with the radiation-limited Γ_1 inferred from the model. Furthermore, we show that our estimate of the quasiparticle density due solely to the ionizing radiation agrees with the observed surplus quasiparticle density in qubits that are well isolated from thermal photons[7,10]. This finding is important for all superconducting applications in which quasiparticle excitations are harmful, such as superconducting quantum computing, superconducting detectors[20–22], or Majorana fermion physics[23].

For emerging quantum processors, one of the most commonly used modalities is the superconducting transmon qubit[24], which comprises one or more Josephson junctions and a shunt capacitor. The intrinsic nonlinear inductance of the junction in combination with the linear capacitance forms an anharmonic oscillator[25]. The non-degenerate transition energies of such an oscillator are uniquely addressable, and in particular, its ground and first excited states serve as the logical $|0\rangle$ and $|1\rangle$ states of the qubit, respectively. In an ideal situation, qubits would suffer no loss of coherence during the run-time of a quantum computation. However, interactions with the environment introduce decoherence channels, which, for the case of energy decay, result in a loss of qubit polarization over time,

$$p(t) = \mathrm{e}^{-\Gamma_1 t}, \tag{1}$$

[1]Massachusetts Institute of Technology, Cambridge, MA, USA. [2]Pacific Northwest National Laboratory, Richland, WA, USA. [3]MIT Lincoln Laboratory, Lexington, MA, USA. [4]Present address: Harvard University, Cambridge, MA, USA. ✉e-mail: avepsala@mit.edu; john.orrell@pnnl.gov

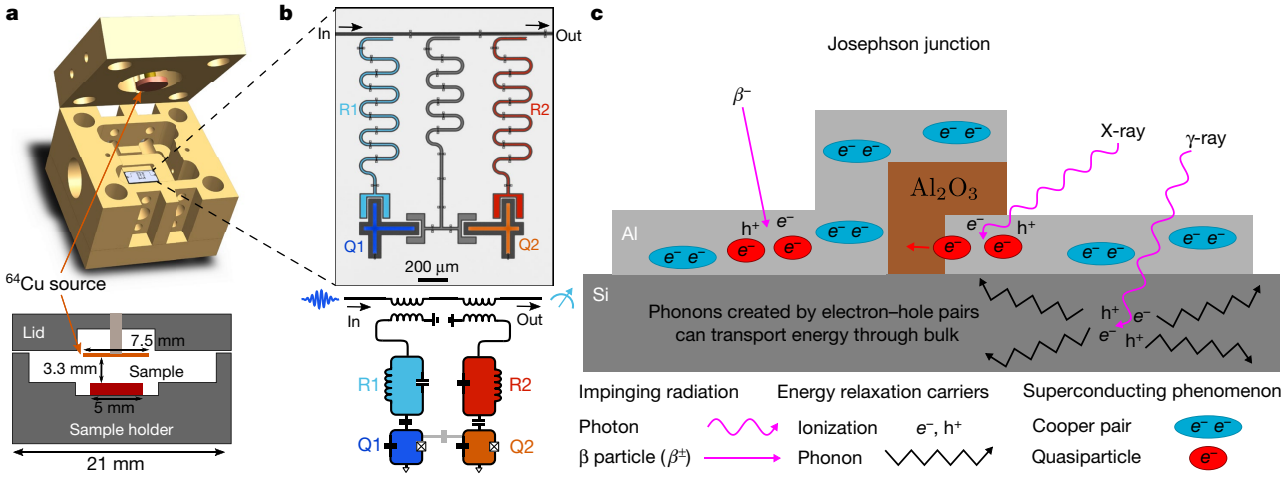

Fig. 1 | Schematic of the experiment. a, Sample holder and ^{64}Cu radiation source. The source is mounted 3.3 mm above the silicon chip containing the superconducting aluminium transmon qubits. **b**, False-colour micrograph and circuit schematic of the qubit sample. The sample consists of two transmon qubits, Q1 (blue, left) and Q2 (orange, right). The resonators used to read out the qubits are shown with red and cyan. The resonators are inductively coupled to a common microwave transmission line, through which both qubit control and readout pulses are sent. The control pulses and the measurement pulses are generated by microwave sources and arbitrary waveform generators at room temperature (not shown here; see Extended Data Fig. 1e). **c**, Diagram of the possible quasiparticle generation processes. Incoming ionizing radiation (from β particles, γ-rays and cosmic rays) interact with the Al qubit and Si substrate, creating electron–hole pairs due to the ionization of atoms and phonons (see text). Beta particles create electron–hole pairs continuously near the surface of dense materials. X-rays also interact with the surface, whereas γ-rays penetrate deeply. The subsequent energy cascade of these electron–hole pairs ultimately breaks Cooper pairs and thereby generates quasiparticles.

where $p(t)$ is the excited-state probability and $\Gamma_1 \equiv 1/T_1$ is the energy-relaxation rate corresponding to the relaxation time T_1, which limits the qubit coherence time. For such processes, the total energy-relaxation rate is a combination of all independent rates affecting the qubit,

$$\Gamma_1 = \Gamma_{qp} + \Gamma_{other}, \quad (2)$$

where Γ_{qp} is the energy-relaxation rate due to the quasiparticles and Γ_{other} contains all other loss channels, such as radiation losses, dielectric losses, and the effect of two-level fluctuators in the materials[26]. In the transmon, the quasiparticle energy-relaxation rate Γ_{qp} depends on the normalized quasiparticle density $x_{qp} = n_{qp}/n_{cp}$ (where n_{qp} is the quasiparticle density and n_{cp} is the Cooper-pair density) and the frequency of the qubit, ω_q, such that[27]

$$\Gamma_{qp} = \sqrt{\frac{2\omega_q \Delta}{\pi^2 \hbar}} x_{qp}. \quad (3)$$

The Cooper pair density and the superconducting gap (Δ) are material-dependent parameters, and for thin-film aluminium they are $n_{cp} \approx 4 \times 10^6\ \mu m^{-3}$ and $\Delta \approx 180\ \mu eV$. This relation allows us to use the energy-relaxation time of a transmon as a sensor for quasiparticle density in the superconductor as well as to estimate the maximum energy-relaxation time of a transmon given a certain quasiparticle density. The thermal equilibrium contribution to x_{qp} is vanishingly small at the effective temperature of the sample, $T_{eff} \approx 40$ mK, compared with the other generation mechanisms that we shall consider here.

Currently, there exists no quantitative microscopic model directly connecting interactions of ionizing radiation (such as β particles, γ-rays and X-rays) to quasiparticle populations in superconductors. However, a phenomenological picture describing the processes involved in this connection is shown in Fig. 1c. The energy of ionizing radiation absorbed in the aluminium metal and silicon substrate is initially converted into ionization electron–hole pairs. We purposely distinguish these high-energy excitations due to the ionization of atoms—which occur in both aluminium and silicon—from the lower-energy quasiparticle excitations resulting from broken Cooper pairs in aluminium. Thereafter, a non-equilibrium relaxation cascade involving secondary ionization carrier and phonon production serves to transfer the absorbed radiation power to and within the aluminium qubit, where it breaks Cooper pairs and generates quasiparticles[28,29].

To estimate the effect of the radiation intensity measured in the laboratory, we use a radiation transport simulation (see Methods for details) to calculate the total quasiparticle-generating power density P_{tot} close to the qubit due to radiation sources. We use a simple model for quasiparticle dynamics[27],

$$\dot{x}_{qp}(t) = -r x_{qp}^2(t) - s x_{qp}(t) + g, \quad (4)$$

where g is the quasiparticle generation rate, which linearly depends on P_{tot}, r is the recombination rate and s is the quasiparticle trapping rate. A steady-state solution for the quasiparticle density is given by $x_{qp} = [-s + (s^2 + 4rg)^{1/2}]/2r$ and if quasiparticle trapping is neglected ($s = 0$), then $x_{qp} = (g/r)^{1/2}$. In a separate quasiparticle injection experiment, we verified that this is a valid approximation in our devices (see Extended Data Fig. 2 and Supplementary Information for discussion). By substituting the model for x_{qp} into equation (3) and using equation (2), the qubit decay rate is given by

$$\Gamma_1 = a\sqrt{\omega_q P_{tot}} + \Gamma_{other}, \quad (5)$$

where a is a coefficient accounting for unknown material parameters and the conversion from absorbed radiation power to quasiparticle generation rate. In addition to the materials of the chip, the conversion efficiency depends on the phononic losses and the thermalization of the sample. The value of a can be experimentally determined by exposing the qubit to a known source of ionizing radiation.

Radiation exposure experiment

To quantify the effect of ionizing radiation on superconducting qubits and to measure the coefficient a in equation (5), we inserted a ^{64}Cu radiation

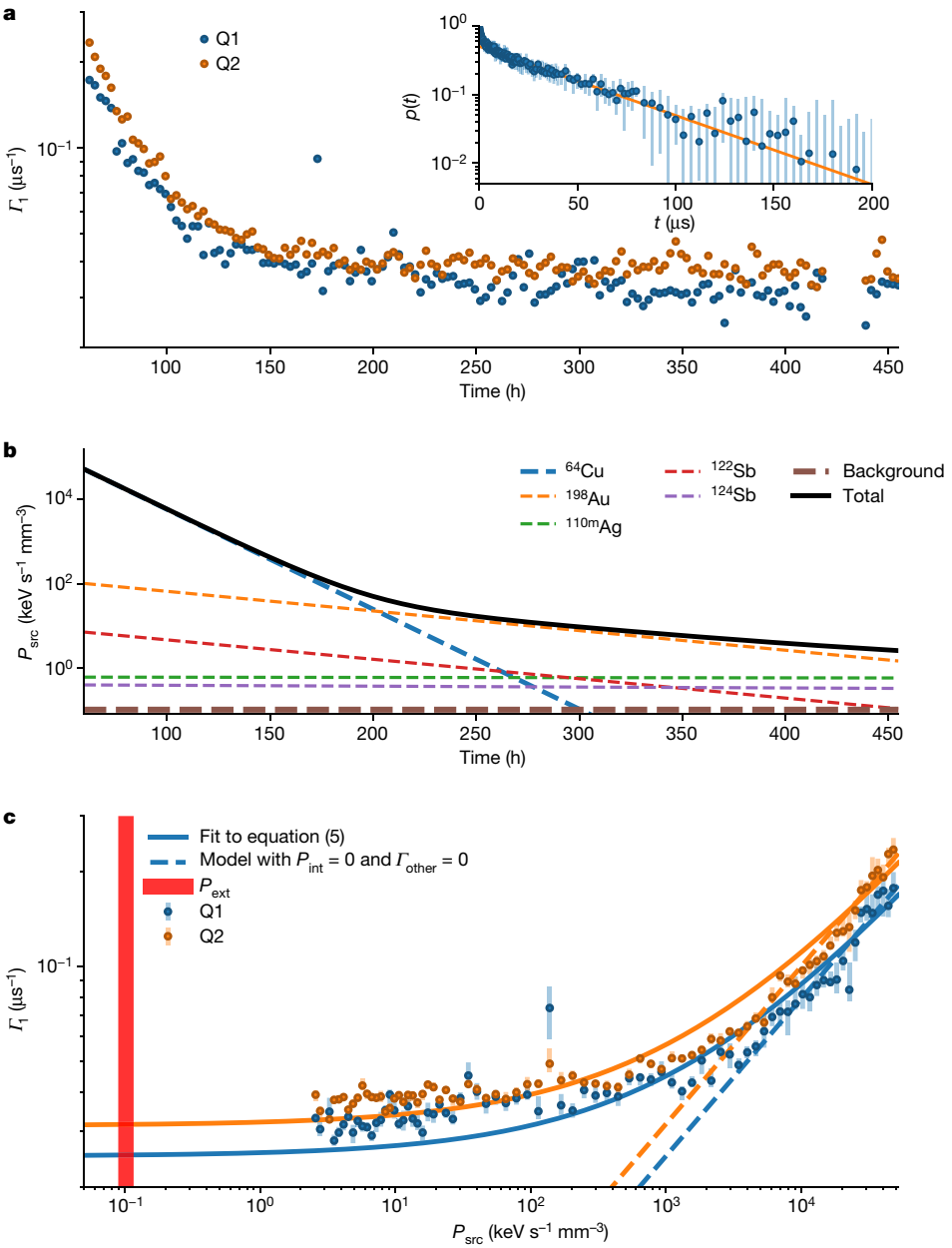

Fig. 2 | Copper-64 radiation exposure experiment. a, Measured energy-relaxation rates $\Gamma_1 = 1/T_1$ of qubits Q1 and Q2 as a function of time when exposed to the ^{64}Cu source. The inset shows an example of the raw data used for fitting the energy-relaxation rates. Blue points are the median of 20 measured qubit excited-state populations $p(t)$ at various times after the excitation pulse. Blue bars indicate the 95% confidence interval (CI) for the median. The orange line is the exponential fit to the data, given in equation (1). The super-exponential decay at short measurement times results from statistical fluctuations in the quasiparticle-induced energy-relaxation rate during the 20 measurements[40]. **b**, Power density of the radiation during the experiment derived from radiation transport simulations (see text). **c**, Energy-relaxation rates Γ_1 as a function of radiation power density. The solid lines show the fit to the model of equation (5). The dashed lines show the fit to model of equation (5) with $\Gamma_{other} = 0$ and $P_{int} = 0$. The vertical red line is the radiation power density due to the external radiation P_{ext}.

source in close proximity to a chip containing two transmon qubits, Q1 and Q2, with average energy-relaxation rates of $\Gamma_1^{(Q1)} = 1/40\ \mu s^{-1}$ and $\Gamma_1^{(Q2)} = 1/32\ \mu s^{-1}$, and transition frequencies $\omega_q^{(Q1)} = 2\pi \times 3.48$ GHz and $\omega_q^{(Q2)} = 2\pi \times 4.6$ GHz (see Fig. 1a, c). Copper-64 has a short half-life of 12.7 h, which permits an observation of the transition from elevated ionizing radiation exposure to normal operation conditions within a single cooldown of the dilution refrigerator. Copper-64 was produced by irradiating high-purity copper foil in the MIT Nuclear Reactor Laboratory (see Methods for details).

The energy-relaxation rate Γ_1 of both qubits was repeatedly measured for over 400 h during the radioactive decay of the ^{64}Cu source (see Fig. 2a, Methods and Extended Data Fig. 3b). During this interval of time, the energy-relaxation rate $\Gamma_1^{(Q1)}$ of Q1 decreased from 1/5.7 μs^{-1} to 1/35 μs^{-1} owing to the gradually decreasing radioactivity of the source, and similarly for Q2. The half-life was long enough to measure individual Γ_1 values at essentially constant levels of radioactivity, yet short enough to sample Γ_1 over a wide range of radiation powers, down to almost the external background level. In addition to affecting qubit energy-relaxation time, the resonance frequencies ω_r of the readout resonators shifted owing to quasiparticle-induced changes in their kinetic inductance, consistent with the quasiparticle recombination model of equation (4). Similarly, we observed a slight shift in the qubit

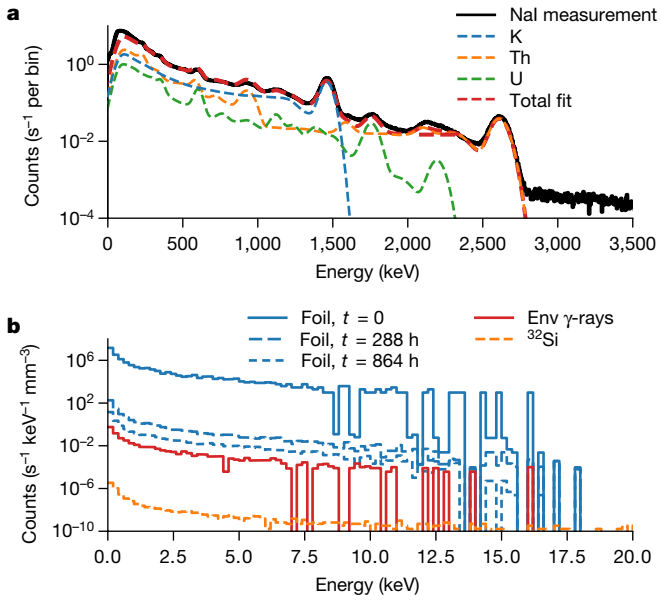

Fig. 3 | Environmental radioactivity assessment. a, Spectrum of γ-radiation in the laboratory measured with NaI scintillation detector, binned in 8,192 energy bins. The data are fitted to the weighted sum of simulated spectra from ^{238}U, ^{232}Th and ^{40}K progenitors convolved with a response function of the NaI detector. These isotopes are typical contaminants in concrete. **b**, Simulated spectral density of power absorbed in the aluminium film that comprises the qubit, calculated with Geant4 using the measured spectrum shown in **a** and the emission spectra of the ^{64}Cu source and its impurities. At $t = 0$, the spectrum is dominated by ^{64}Cu, after 12 days by ^{198}Au impurities, and after 36 days by ^{110m}Ag (m, metastable). Silicon-32 is a radioactive contaminant intrinsic to the silicon substrate[33]. The fluctuations in the simulated spectra are due to finite simulation statistics. Env, environmental.

frequencies and a reduced T_2 time (see Supplementary Information and Extended Data Figs. 4, 5).

The intensity of the radiation source used in the experiment was calibrated as a function of time by using the γ-ray spectroscopy of a reference copper foil that had been irradiated concurrently. The foils included a small amount of longer-lived radioactive impurities that began to noticeably alter the radiated power density expected for ^{64}Cu about 180 h into the measurements (see Fig. 2b). For both the ^{64}Cu and the long-lived impurities, the radiation intensities from the different isotopes were converted to a single power density of ionizing radiation by using the radiation transport simulation package Geant4[30,31] (see Methods for details). The contributions of the different isotopes (dashed lines) and the resulting net power density (solid line) of the radiation from the source, P_{src}, are shown in Fig. 2b over the measurement time window.

Using the data in Fig. 2b as a method for calibrated time–power conversion, the energy-relaxation rates of qubits Q1 and Q2 are presented as a function of the radiation power density P_{src} (Fig. 2c). In the high-P_{src} limit (short times), the model of equation (5) can be fitted to the data to extract the value for the conversion coefficient $a = 5.4 \times 10^{-3}$ (mm^3 keV^{-1})$^{1/2}$ by assuming that $P_{tot} \approx P_{src}$ dominates all radiation sources that generate quasiparticles as well as all other decay channels. In the low-P_{src} limit (long times), the qubit energy-relaxation rate is limited predominantly by the decay rate Γ_{other} and, to a lesser extent, by the long-lived radioactive impurities in the foil.

Having determined the coefficient a in equation (5), we now remove the calibrated radiation source. In its absence, the total radiation power density that generates quasiparticles can be categorized into two terms, $P_{tot} = P_{int} + P_{ext}$. The term P_{int} accounts for radiation power sources that are internal to the dilution refrigerator, such as infrared photons from higher-temperature stages or radioactive impurities present during the manufacturing of the refrigerator components. P_{ext} is the external ionizing radiation source outside the dilution refrigerator whose influence on the qubits we attempt to determine in the shielded experiment described in the next section. To estimate the contribution of external radiation power P_{ext} to the data shown in Fig. 2, we directly measured the energy from the radiation fields present in the laboratory arising from γ-rays (see Fig. 3) and cosmic rays, including those due to secondary processes such as muon fields, by using a NaI radiation detector (see Methods and Extended Data Fig. 6e). The spectra were used to determine the radiation intensities from cosmic rays and naturally occurring radioactive isotopes in the laboratory. These measured intensities were then used in a Geant4 radiation transport simulation to estimate the total external power density $P_{ext} = 0.10 \pm 0.02$ keV mm^{-3} s^{-1} deposited in the aluminium that constitutes the resonators and qubits. About 60% of the external radiation power density results from the radioactive decays within the concrete walls of the laboratory (0.06 keV mm^{-3} s^{-1}), with cosmic rays contributing the remaining 40% (0.04 keV mm^{-3} s^{-1}). This external power level is indicated with a vertical red band in Fig. 2c. Although statistical errors in the measured intensities are small, we find a combined systematic uncertainty of approximately 20%. The contributions of different sources to the total systematic uncertainty are detailed in Methods.

Using the model in equation (5) with the determined parameters for a and P_{ext} and the known qubit frequencies, we find that the lower limit on the total energy-relaxation rate due to the external radiation P_{ext} in the absence of all other energy-relaxation mechanisms is $\Gamma_1^{(Q1)} \approx 1/3,950\ \mu s^{-1}$ and $\Gamma_1^{(Q2)} \approx 1/3,130\ \mu s^{-1}$, corresponding to where the dashed lines would intersect the vertical red band in Fig. 2c. These rates correspond to the point at which naturally occurring radiation from the laboratory would become the dominant limiting contributor to the qubit energy-relaxation rate. Although its effect on the energy-relaxation time is not dominant for today's qubits, ionizing radiation will need to be considered when aiming for the coherence times required for fault-tolerant quantum computing. We can furthermore apply equation (3) to estimate the quasiparticle density caused by the ionizing radiation background, giving $x_{qp} \approx 7 \times 10^{-9}$, which agrees well with the lowest reported excess quasiparticle densities[10].

Shielding experiment

We sought to verify the above result by shielding the qubits with 10-cm-thick lead bricks outside the cryostat to reduce the external radiation and thereby improve the qubit energy-relaxation times (see Fig. 4). The shield was built on a scissor lift so that we could cyclically raise and lower it to perform an A/B test of its effect. By using the parameters extracted from the radiation exposure measurement and the model in equation (5), the expected improvement of the energy-relaxation rate due to the shield can be estimated from

$$\delta\Gamma_1 \equiv \Gamma_1^{d} - \Gamma_1^{u} = a\sqrt{\omega_q}\left(\sqrt{P_{int} + (1-\eta^{d})P_{ext}} - \sqrt{P_{int} + (1-\eta^{u})P_{ext}}\right), \quad (6)$$

where η is the fraction of ionizing radiation blocked by the shield, and the label u (d) corresponds to the parameters when the shield is up (down). We can make a realistic estimate of the efficiency of the shield by measuring the radiation energy spectrum with and without the shield using a NaI detector, giving $\eta^{u} = 46.1\%$. The shield blocks approximately 80% of the radiation from the nuclear decay events in the laboratory but is inefficient against the cosmic rays (see Methods for details). From equation (6), in the absence of internal radiation sources ($P_{int} = 0$), the expected effect of the shield on the energy-relaxation rate of Q1 is $\delta\Gamma_1 \approx 1/15.5\ ms^{-1}$, which is only 0.26% of the energy-relaxation rate of qubit Q1.

To detect a signal this small, we measured the energy-relaxation rates of the qubits while periodically placing the shield in the up and down

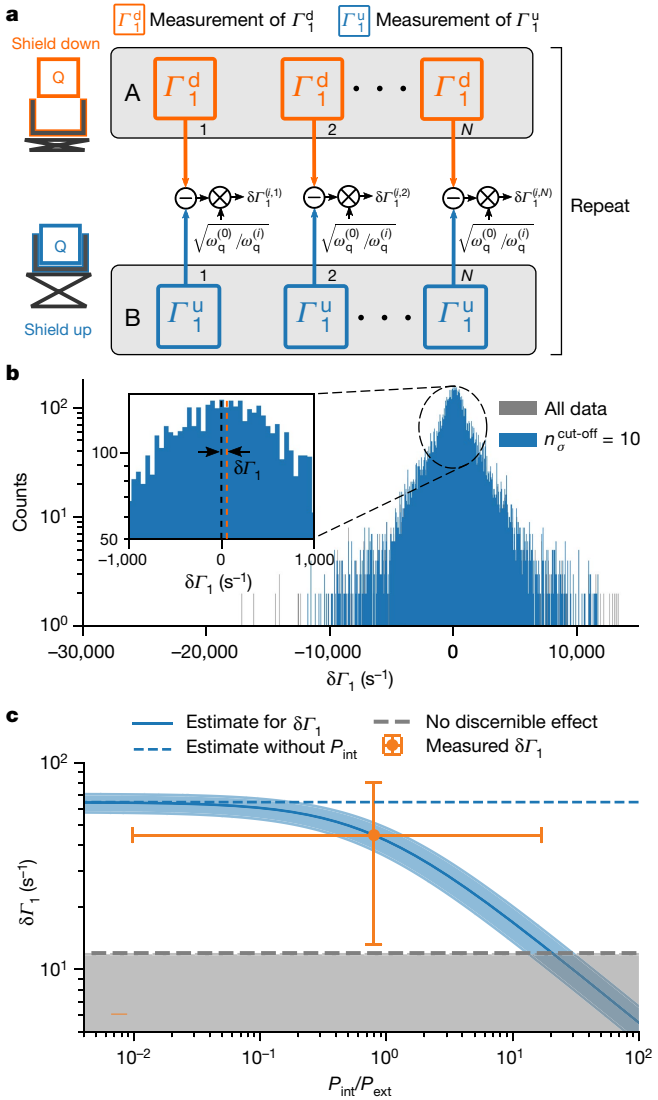

Fig. 4 | Qubit shielding experiment. a, Schematic of shielding experiment. The qubit energy-relaxation rate is measured N times with the shield up and then again N times with the shield down. This cycle is repeated 65 times for qubits Q1 and Q2, and 85 times for qubits Q3–Q7. **b**, Histogram of the differences in energy-relaxation rates when the shield is up versus down. The inset shows the histogram peak. The orange vertical line indicates the median of the distribution. Although the median difference in the relaxation rates between shield-up and shield-down configurations is only 1.8% of the width of the distribution, it differs from zero in a statistically significant manner. **c**, Difference in the energy-relaxation rates in the shielding experiment (orange dot) versus $P_{\text{int}}/P_{\text{ext}}$. Vertical error bars show the 95% CI for the median of $\delta\Gamma_1$. Horizontal error bars are the corresponding CIs for P_{int}. The blue line indicates the energy-relaxation rate estimated using the model from the ^{64}Cu radiation exposure measurement and equation (6). The shaded blue region shows the CI for the estimate, assuming ±20% relative error for P_{ext}. Below the grey dashed line, the experiment is not sensitive enough to detect $\delta\Gamma_1$.

positions and then comparing their difference over many cycles, similar in spirit to a Dicke switch radiometer measurement[32] (see Fig. 4a for a schematic). A single up/down cycle of the lead shield lasted 15 min. To accelerate the data acquisition, we installed an additional sample in the dilution refrigerator with five qubits similar to Q1 and Q2.

Figure 4b shows the histogram of the accumulated differences in the energy-relaxation rates, $\delta\Gamma_1$, for all of the qubits over the entire measurement, normalized to the frequency of Q1 using equation (5). From the median of the histogram, we estimate the shift in the energy-relaxation rate $\delta\Gamma_1 = 1/22.7\ \text{ms}^{-1}$, 95% CI [1/75.8, 1/12.4] ms^{-1}. The Wilcoxon signed-rank test can be used to assess if the measured energy-relaxation rates are lower in the shield up than in the shield down positions, and it yields a P-value of 0.006. As the P-value is much less than 0.05, we can reject the null hypothesis that the shield did not have any effect on the qubit energy-relaxation time with high confidence (see Methods and Extended Data Fig. 7 for additional details on the statistical analysis).

In Fig. 4c, we have compared the result of the shielding experiment to the estimate of the effect of the background radiation obtained from the radiation exposure measurement. The orange dot shows $\delta\Gamma_1$ extracted from the shielding experiment. The solid blue line shows how this value would trend based on the predicted effect of the shield at the given P_{ext} measured in the laboratory for different values of internal radiation power density P_{int}. Although we do not know the exact value of P_{int}, we can approximate it by substituting the measured $\delta\Gamma_1$ and a into equation (6) and by solving for $P_{\text{int}} \approx 0.081\ \text{keV mm}^{-3}\ \text{s}^{-1}$, 95% CI [0, 1.73] $\text{keV mm}^{-3}\ \text{s}^{-1}$. This value for P_{int}, along with P_{ext}, corresponds to a total quasiparticle density $x_{\text{qp}} \approx 1.0 \times 10^{-8}$, again consistent with earlier observations[10].

Despite the uncertainty in the specific value of P_{int}, the results acquired from the two independent experiments agree remarkably well. We conclude that, in the absence of all other energy-relaxation mechanisms, the ionizing radiation limits the qubit energy-relaxation rate to $\Gamma_1 \approx 1/4\ \text{ms}^{-1}$. In turn, shielding the qubits from environmental ionizing radiation improved their energy-relaxation time. The observed energy-relaxation rate was reduced by $\delta\Gamma_1 \approx 1/22.7\ \text{ms}^{-1}$, which is an 18% improvement over the radiation-induced Γ_1 of the qubits. The shield was not able to remove all of the effects of the radiation, owing to both the presence of internal radiation P_{int} and the imperfect efficiency of the shield.

Discussion

The first reported results of the systematic operation of superconducting transmon qubits under intentionally elevated levels of ionizing radiation clearly show a deleterious effect on the performance of the qubits. We quantitatively determined the impact of radiation power density on the qubit energy-relaxation time and showed that naturally occurring ionizing radiation in the laboratory creates excess quasiparticles in superconductors, reducing the qubit energy-relaxation time.

By using shielding techniques commonly applied in neutrino physics and the search for dark matter[33–39], we improved the energy-relaxation rate of our qubits by approximately 0.2%. Although a rather small improvement for today's qubits, which are currently limited by other relaxation mechanisms, a simple model of the ionization generation of quasiparticles indicates that transmon qubits of this design will need to be shielded against ionizing radiation—or otherwise redesigned to mitigate the impact of its resulting quasiparticles—to reach energy-relaxation times in the millisecond regime. Additionally, as was recently done with resonators[19], locating qubit systems deep underground where cosmic rays and cosmogenic activation are greatly reduced should provide benefits for advancing quantum computing research.

Our results also shed light on a decades-old puzzle, namely the origin of non-equilibrium quasiparticles widely observed in experiments with superconductors at millikelvin temperatures. Our measurements indicate that ionizing radiation accounts for a considerable fraction of the residual excess quasiparticle levels observed in otherwise carefully filtered experiments, with impact on many fields that use superconducting circuitry. For example, excess quasiparticles reduce the sensitivity of kinetic inductance detectors and transition edge sensors used in astronomy. Additionally, quasiparticle poisoning is a major impediment facing topologically protected Majorana fermions. Identifying ionizing radiation as a dominant source of excess quasiparticles

is a first step towards developing techniques—such as lead shielding, quasiparticle trapping, and designing devices with reduced quasiparticle sensitivity—to mitigate its impact on superconducting circuits, including those used for quantum computation.

Online content

Any methods, additional references, Nature Research reporting summaries, source data, extended data, supplementary information, acknowledgements, peer review information; details of author contributions and competing interests; and statements of data and code availability are available at https://doi.org/10.1038/s41586-020-2619-8.

1. DiVincenzo, D. The physical implementation of quantum computation. *Fortschr. Phys.* **48**, 771–783 (2000).
2. Arute, F. et al. Quantum supremacy using a programmable superconducting processor. *Nature* **574**, 505–510 (2019).
3. Kandala, A. et al. Error mitigation extends the computational reach of a noisy quantum processor. *Nature* **567**, 491–495 (2019).
4. Lutchyn, R., Glazman, L. & Larkin, A. Kinetics of the superconducting charge qubit in the presence of a quasiparticle. *Phys. Rev. B* **74**, 064515 (2006).
5. Martinis, J. M., Ansmann, M. & Aumentado, J. Energy decay in superconducting Josephson-junction qubits from nonequilibrium quasiparticle excitations. *Phys. Rev. Lett.* **103**, 097002 (2009).
6. Jin, X. et al. Thermal and residual excited-state population in a 3D transmon qubit. *Phys. Rev. Lett.* **114**, 240501 (2015).
7. Serniak, K. et al. Hot nonequilibrium quasiparticles in transmon qubits. *Phys. Rev. Lett.* **121**, 157701 (2018).
8. Aumentado, J., Keller, M. W., Martinis, J. M. & Devoret, M. H. Nonequilibrium quasiparticles and 2*e* periodicity in single-Cooper-pair transistors. *Phys. Rev. Lett.* **92**, 066802 (2004).
9. Taupin, M., Khaymovich, I., Meschke, M., Mel'nikov, A. & Pekola, J. Tunable quasiparticle trapping in Meissner and vortex states of mesoscopic superconductors. *Nat. Commun.* **7**, 10977 (2016).
10. Serniak, K. et al. Direct dispersive monitoring of charge parity in offset-charge-sensitive transmons. *Phys. Rev. Appl.* **12**, 014052 (2019).
11. Córcoles, A. D. et al. Protecting superconducting qubits from radiation. *Appl. Phys. Lett.* **99**, 181906 (2011).
12. Barends, R. et al. Minimizing quasiparticle generation from stray infrared light in superconducting quantum circuits. *Appl. Phys. Lett.* **99**, 113507 (2011).
13. Bespalov, A., Houzet, M., Meyer, J. S. & Nazarov, Y. V. Theoretical model to explain excess of quasiparticles in superconductors. *Phys. Rev. Lett.* **117**, 117002 (2016).
14. Nakamura, Y., Pashkin, Y. A. & Tsai, J. S. Coherent control of macroscopic quantum states in a single-Cooper-pair box. *Nature* **398**, 786–788 (1999).
15. Oliver, W. D. & Welander, P. B. Materials in superconducting quantum bits. *MRS Bull.* **38**, 816–825 (2013).
16. Kjaergaard, M. et al. Superconducting qubits: current state of play. *Annu. Rev. Condens. Matter Phys.* **11**, 369–395 (2020).
17. Gottesman, D. Theory of fault-tolerant quantum computation. *Phys. Rev. A* **57**, 127–137 (1998).
18. Grünhaupt, L. et al. Loss mechanisms and quasiparticle dynamics in superconducting microwave resonators made of thin-film granular aluminum. *Phys. Rev. Lett.* **121**, 117001 (2018).
19. Cardani, L. et al. Reducing the impact of radioactivity on quantum circuits in a deep-underground facility. Preprint at https://arXiv.org/abs/2005.02286 (2020).
20. Day, P. K., LeDuc, H. G., Mazin, B. A., Vayonakis, A. & Zmuidzinas, J. A broadband superconducting detector suitable for use in large arrays. *Nature* **425**, 817–821 (2003).
21. Irwin, K. D., Hilton, G. C., Wollman, D. A. & Martinis, J. M. X-ray detection using a superconducting transition-edge sensor microcalorimeter with electrothermal feedback. *Appl. Phys. Lett.* **69**, 1945–1947 (1996).
22. Moore, D. C. et al. Position and energy-resolved particle detection using phonon-mediated microwave kinetic inductance detectors. *Appl. Phys. Lett.* **100**, 232601 (2012).
23. Albrecht, S. et al. Transport signatures of quasiparticle poisoning in a Majorana island. *Phys. Rev. Lett.* **118**, 137701 (2017).
24. Koch, J. et al. Charge insensitive qubit design derived from the Cooper pair box. *Phys. Rev. A* **76**, 042319 (2007).
25. Krantz, P. et al. A quantum engineer's guide to superconducting qubits. *Appl. Phys. Rev.* **6**, 021318 (2019).
26. Klimov, P. et al. Fluctuations of energy-relaxation times in superconducting qubits. *Phys. Rev. Lett.* **121**, 090502 (2018).
27. Wang, C. et al. Measurement and control of quasiparticle dynamics in a superconducting qubit. *Nat. Commun.* **5**, 5836 (2014).
28. Kozorezov, A. et al. Quasiparticle-phonon downconversion in nonequilibrium superconductors. *Phys. Rev. B* **61**, 11807 (2000).
29. Kozorezov, A., Wigmore, J., Martin, D., Verhoeve, P. & Peacock, A. Electron energy down-conversion in thin superconducting films. *Phys. Rev. B* **75**, 094513 (2007).
30. Allison, J. et al. Geant4 developments and applications. *IEEE Trans. Nucl. Sci.* **53**, 270–278 (2006).
31. Agostinelli, S. et al. Geant4—a simulation toolkit. *Nucl. Instrum. Meth. A* **506**, 250–303 (2003).
32. Dicke, R. The measurement of thermal radiation at microwave frequencies. *Rev. Sci. Instrum.* **17**, 268–275 (1946).
33. Aguilar-Arevalo, A. et al. Search for low-mass WIMPs in a 0.6 kg day exposure of the DAMIC experiment at SNOLAB. *Phys. Rev. D* **94**, 082006 (2016).
34. Agnese, R. et al. Projected sensitivity of the SuperCDMS SNOLAB experiment. *Phys. Rev. D* **95**, 082002 (2017).
35. Alduino, C. et al. First results from CUORE: a search for lepton number violation via $0\nu\beta\beta$ decay of ^{130}Te. *Phys. Rev. Lett.* **120**, 132501 (2018).
36. Agostini, M. et al. Improved limit on neutrinoless double-β decay of ^{76}Ge from GERDA phase II. *Phys. Rev. Lett.* **120**, 132503 (2018).
37. Gando, A. et al. Search for Majorana neutrinos near the inverted mass hierarchy region with KamLAND-Zen. *Phys. Rev. Lett.* **117**, 082503 (2016).
38. Aalseth, C. E. et al. Search for neutrinoless double-β decay in ^{76}Ge with the Majorana demonstrator. *Phys. Rev. Lett.* **120**, 132502 (2018).
39. Albert, J. B. et al. Search for neutrinoless double-beta decay with the upgraded EXO-200 detector. *Phys. Rev. Lett.* **120**, 072701 (2018).
40. Gustavsson, S. et al. Suppressing relaxation in superconducting qubits by quasiparticle pumping. *Science* **354**, 1573–1577 (2016).

Methods

Measurement set-up

Extended Data Fig. 1a shows the measurement set-up used to measure the energy-relaxation times of the qubits. The qubit control pulses are created by a Keysight PXI arbitrary waveform generator. The in-phase and quadrature pulses are up-converted to the qubit transition frequency using single sideband IQ modulation. The readout pulses are created similarly. The control and readout pulses are combined and sent to the sample through a single microwave line. There is a total of 60 dB attenuation in the line to reduce the thermal noise from the room temperature and the upper stages of the dilution refrigerator. In the control line, there are absorbing filters (Eccosorb) before and after the sample, which further reduce the infrared radiation (thermal photons) reaching the qubit. The control line is inductively coupled to readout resonators R1 and R2.

The control pulses are applied to the qubit via the readout resonator, which filters the signal at the qubit frequency. Nonetheless, by using sufficiently large-amplitude pulses, the qubits can be excited in 25 ns.

The qubit state is determined using dispersive readout via a circuit quantum electrodynamics architecture[41]. The dispersive readout is based on the resonator frequency slightly changing depending on the state of the qubit. The change can be detected by using a single measurement tone near the resonator resonance frequency and measuring the transmitted signal in the microwave line. The measurement signal is boosted by a chain of amplifiers. The first amplifier used is a near-quantum-limited travelling-wave parametric amplifier (TWPA), which has a very low noise temperature and gain up to 30 dB (ref. [42]). As with all parametric amplifiers, the TWPA requires a pump tone, which is driven by a signal generator at room temperature. The measurement signal is further amplified by high-electron-mobility transistor (LNF) amplifier, which is thermally anchored to the 3 K stage of the refrigerator. At room temperature, there is a final pre-amplifier followed by a heterodyne detector. The down-converted in-phase and quadrature intermediate-frequency (IF) signals are digitized with a Keysight PXI digitizer (500 MHz sampling rate) and then further digitally demodulated using a field-programmable gate array integrated in the the digitizer to extract the measured qubit state. Measurement results are ensemble-averaged over many such trials to infer the occupation probability of the qubit being in a given state.

In the experiments, we used one sample with two transmon qubits, and a second sample with five transmon qubits. The qubits were fabricated using optical and electron-beam lithography. By construction, the structure of our qubits is kept simple and pristine—aluminium grown in a high-vacuum molecular beam epitaxy (MBE) chamber on top of high-resistivity silicon—to reduce defects that cause decoherence. The Josephson junctions have an additional layer of aluminium oxide in between the aluminium leads and are fabricated using double-angle shadow evaporation in another ultra-high-vacuum evaporator (different from the MBE). The fabrication is similar to that described in ref. [43].

The table in Extended Data Fig. 1e shows the relevant qubit parameters. The reported energy-relaxation times are median values during the lead shield experiment. The values for the energy-relaxation rates of Q1 and Q2 differ from those reported for ^{64}Cu measurements because of their fluctuation over time.

Production of ^{64}Cu source

The ^{64}Cu radiation source was created by neutron activation of natural copper via the capture process ^{63}Cu(n,γ)^{64}Cu. Given its 12.7-h half-life, ^{64}Cu is well suited for deployment in a dilution refrigerator, since it takes 72–100 h to cool to base operating temperature. In the irradiation, we took into account the anticipated ^{64}Cu decay during the cool-down period, by specifically irradiating at higher levels of ^{64}Cu than used in the qubit study and then allowing the foils time to decay to lower levels of activity.

Two copper disks created from the same McMaster-Carr foil were irradiated with neutrons at the MIT Reactor (MITR). The two foils are referred to as sample A and A-Ref. The irradiated sample A was installed in the dilution refrigerator with the two qubits described in this study, while A-Ref was kept to determine the level of radioactive activation products. Each of the foils was 7.5 mm in diameter and 0.5 ± 0.1 mm thick. Samples A and A-Ref had a mass of 178.5 mg and 177.6 mg, respectively. The total neutron irradiation exposure was 7 min and 14 s in duration. With a high-purity γ-ray spectrometer, the A-Ref sample was used to determine the ^{64}Cu activation level. We determine the activity of sample A to be 162 ± 2 μCi at 9:00 a.m. ET, 13 May 2019. This activity is based on measurements of 1,346-keV γ-rays from ^{64}Cu using a high-purity germanium (HPGe) counter.

Despite the high copper purity (99.99%), trace elements with high neutron cross-sections can also be activated from the neutron irradiation process. The same HPGe counter was used to determine the presence of other trace elements, the results of which are reported in Extended Data Fig 6a.

Operation of NaI detector

A standard commercial NaI detector measures energy deposited in the NaI crystal through the scintillation light created when γ-rays or X-rays scatter atomic electrons in the crystal. The magnitude of the scintillation light signal, measured by a photomultiplier tube (PMT), is proportional to the energy deposited in the NaI crystal by the incident radiation. As the specific energy of γ-rays or X-rays are indicative of the radioactively decaying nucleus, an energy spectrum measured by the NaI detector can be used to determine the relative contributions of ionizing radiation in the laboratory due to different naturally occurring radioactive isotopes. In a normal laboratory environment, the dominant naturally occurring radioactive nuclei consist of isotopes in the uranium (^{238}U) and thorium (^{232}Th) decay chains as well as ^{40}K. These features are identified in Fig. 3a.

It is possible to reduce the high voltage applied to the PMT, effectively reducing the gain on the scintillation light signal from the NaI detector. This enables the measurement of ionizing cosmic rays—and the secondary radiation produced by them—as determined mainly by spectral features above 2.7 MeV (ref. [44]) (see Extended Data Fig 6e for the measured spectrum). We can fit the known spectrum of cosmic rays to the measured spectrum to find the cosmic-ray flux in the laboratory. The fit is shown in Extended Data Fig 6e. Note that, below 2.7 MeV, the large difference between the measurement and the fit is due to the radiation from nuclear decays, as shown in Fig. 3a.

Radiation transport simulations and normalization

To estimate the power density imparted into the qubits by radiation, we developed a radiation transport simulation. The simulation was performed with the Geant4 toolkit[31] which is designed for modelling the interaction of radiation and particles with matter. The simulation geometry included a detailed model of the layers of the Leiden cryogenics CF-CS81 dilution refrigerator, the mounting fixtures and containment for the qubit, and the activated copper foil as it was located for the experiment. The qubit chip is modelled as a 380-μm-thick piece of silicon with a 200-nm aluminium cladding. Input power density is estimated by measuring simulated energy deposited into the aluminium layer. Three separate radiation source terms are considered: ^{64}Cu and the other isotopes in the activated copper foil; naturally occurring background radiation primarily from the concrete walls of the laboratory; and cosmic-ray muons.

To estimate the effect of isotopes in the copper, we make use of the radioactive decay simulation capabilities of Geant4. Instances of each isotope are distributed uniformly throughout the simulated foil volume. Geant4 samples the available decay modes for that isotope with appropriate branching fractions, and generates the corresponding secondary particles (γ-rays, β particles, positrons and so on), which

are then tracked until they have deposited all their energy. By tallying these events, we can estimate the average input energy density into the qubit substrate per decay, or equivalently the average power density per unit of isotope activity. The total simulated spectrum at various times during the qubit measurement campaign are shown in Fig. 3b.

To understand the background levels of ionizing radiation present in the MIT laboratory where all qubit devices are operated, a 3″ × 3″ NaI scintillator detector was deployed near the dilution refrigerator where the qubit measurements were made. The detector was represented in the radiation transport simulation as a bare NaI cylinder (not including any housing, PMT and so on). γ-rays with an energy spectrum following the equilibrium emissions of the most common radioactive isotopes (^{238}U, ^{232}Th and ^{40}K) are simulated starting in a sphere surrounding the NaI detector with an isotropic initial direction. A small number of simulations were run with different-sized initial locations to evaluate the impact of this parameter, yielding a 10% systematic uncertainty.

To fit to the measured data, the simulated energy deposits must be broadened to account for the detector's finite energy resolution. We used a quadratic energy-scaling function to map energy to measured analogue-to-digital converter counts, and a quadratic resolution function as a function of energy:

$$\sigma^2 = \sigma_0^2 + \sigma_1^2 E + \sigma_2^2 E^2 \tag{7}$$

Each of the energy scale and resolution coefficients is left free in the fit, as well as the flux of each isotope, for a total of nine free parameters. The result for a fit over the range 0.2–2.9 MeV is shown in Fig. 3a. The fit is much better when performed over a narrower region of the data. This could be improved with a more sophisticated response function, but we address the issue by performing the fit separately over three energy ranges, 0.2–1.3 MeV, 1.3–2.9 MeV and 0.2–2.9 MeV, and taking the difference as a systematic uncertainty. This result is reported in the first line of the table in Extended Data Fig 6b. In total, the uncertainty in the fits contributes 8% to the systematic uncertainty. The simulated energy deposition efficiency for each external isotope is approximately equal to 0.04 keV s^{-1} mm^{-3} per (cm^{-2} s^{-1}), which yields a total power density from environmental γ-rays of 0.060 ± 0.005 keV s^{-1} mm^{-3}.

The same NaI detector, operated at lower gain, is used to estimate the cosmic-ray flux (see Extended Data Fig 6e). Cosmic-ray muons are simulated in a 1-m square plane above the detector, using the CRY package to generate the energy spectrum and angular distribution[45]. The muon flux taken directly from CRY is 1.24 × 10^{-2} cm^{-2} s^{-1}. A fit to the low-gain NaI data, using the same convolutional technique as for γ-rays, yields (9.7 ± 0.1) × 10^{-3} cm^{-2} s^{-1}, or about 20% lower than the CRY value. The same simulation gives an energy deposition efficiency in the qubits of 4.3 ± 0.2 keV s^{-1} mm^{-3} per (cm^{-2} s^{-1}) of cosmic-ray muon flux. This, in turn, yields a cosmic-ray-induced power density of 0.042 ± 0.002 keV s^{-1} mm^{-3}.

Throughout this work, we have based our analysis on the absorbed power density in the aluminium. However, radiation will also interact with and deposit energy in the silicon substrate. How much of this energy, if any, reaches the aluminium layer and is converted to quasiparticles is unknown, in part because we do not know the relevant coupling rates between silicon and aluminium or the various recombination rates of the quasiparticles. This motivated our use of a calibrated ^{64}Cu source, which we use to parameterize the net effect. In fact, as we show below, whether we consider aluminium only, or aluminium plus silicon, the difference in the net result changes by at most order unity. This counterintuitive result arises because the power densities in aluminium and silicon are approximately the same, and because the ^{64}Cu captures the net effect in either case.

Although ^{64}Cu captures the net effect well, small differences arise due to how the radiation is emitted and absorbed. For example, in comparison to highly penetrating radiation, ^{64}Cu deposits a larger fraction of its emitted energy into the aluminium, because a larger fraction is emitted as β particles. If the quasiparticle density is dominated by energy from the silicon rather than the aluminium, the relative strength of ^{64}Cu to the other trace activated isotopes would be approximately 60% lower. The external power density induced from environmental γ-rays is approximately 20% lower, whereas the cosmic-ray power density is 13% higher, for a net 7% total increase in external power. The lead shielding effectiveness (η) is also approximately 15% higher for the silicon than aluminium. By choosing aluminium, we are taking the most conservative estimate for the impact of environmental radiation on qubit energy relaxation.

We now show that these differences are at most an effect of order unity. If, for example, the quasiparticle generation rate is dominated by the total absorbed power in the silicon substrate, we can estimate the maximal relative error in the estimate of Γ_1 by comparing the ratios of the power densities of the external radiation P_{ext} absorbed in the aluminium film and the silicon substrate to the ratios of power densities induced by the ^{64}Cu source as

$$f_{\mathrm{c}} = \sqrt{\frac{P_{\mathrm{src}}^{\mathrm{Al}}(t)}{P_{\mathrm{src}}^{\mathrm{Si}}(t)} \times \frac{P_{\mathrm{ext}}^{\mathrm{Si}}}{P_{\mathrm{ext}}^{\mathrm{Al}}}} \approx 1.6. \tag{8}$$

This would increase our estimate of the effect of the external radiation on the qubit energy-relaxation rate from $\Gamma_1^{(\mathrm{Q1})} = 1/4\ \mathrm{ms}^{-1}$ to $\Gamma_1^{(\mathrm{Q1})} = a\sqrt{\omega_{\mathrm{q}}^{(\mathrm{Q1})} P_{\mathrm{ext}} f_{\mathrm{c}}} \approx 1/2.5\ \mathrm{ms}^{-1}$. See Supplementary Information for the derivation of the above formula. Note that the calculation is an upper-limit estimation, which would be reached only if the total phonon coupling between the silicon substrate and the aluminium were much stronger than the coupling between the sample and the sample holder.

Measurement of the qubit energy-relaxation rate

At the beginning of the measurement, all the qubits are initialized in their ground states. Owing to the finite temperature of their environment and hot quasiparticles[6,7], there is a small excited-state population, approximately 1.7% for these qubits and their qubit transition frequencies. This corresponds to an effective temperature $T_{\mathrm{eff}} \approx 40$ mK (ref. [6]). At this temperature, the thermal quasiparticle population can be estimated to be

$$x_{\mathrm{qp}}^{\mathrm{thermal}} = \sqrt{2\pi \frac{k_{\mathrm{B}} T}{\Delta}}\ \mathrm{e}^{-\frac{\Delta}{k_{\mathrm{B}} T}} \approx 7 \times 10^{-24}. \tag{9}$$

It is interesting to note that the quasiparticle density $x_{\mathrm{qp}} \approx 7 \times 10^{-9}$ due to environmental ionizing radiation (as inferred from our ^{64}Cu measurements) would correspond to an equilibrium quasiparticle temperature $T \approx 120$ mK—consistent with the temperature below which qubit parameters such as T_1 stop following an equilibrium quasiparticle model in previous experiments (around 150 mK; see, for example, refs. [7,40]).

The qubit energy-relaxation rate Γ_1 is measured by first driving the qubits to their first excited state using a microwave π-pulse (see Extended Data Fig. 3b). The state of all the qubits is measured simultaneously after time t, which gives an estimate for their residual excited-state population $p(t)$. By changing t, the time evolution of the populations can be determined. The model described in equation (2) in the main text can be fitted to the measured data to find the energy-relaxation rate Γ_1 of the qubits.

Estimating the internal radiation rate P_{int}

An accurate estimate of the internal radiation rate P_{int} is important for comparing the feasibility of the shielding effect of the lead shield to the estimated effect of the external radiation power density on the change in qubit energy-relaxation rate $\delta\Gamma$ extracted from the ^{64}Cu experiment. A simple way of making the estimate is to extract it from

the fit to the data in Fig. 3c. However, the accuracy of the estimate is relatively low, as it is difficult to separate P_{int} from the energy-relaxation rate of the qubit due to sources other than quasiparticles, Γ_{other}. In principle, it is possible to distinguish the two sources, because according to equation (4), the scaling of Γ_1 is proportional to $\sqrt{P_{\mathrm{ext}}+P_{\mathrm{int}}+P_{\mathrm{src}}}$ whereas the internal energy-relaxation rate Γ_{other} contributes linearly to Γ_1 (see equation (2)). In practice, this is inaccurate, especially if quasiparticle loss is not the dominating loss-mechanism.

Instead, we use the shielding experiment to calculate an upper bound for P_{int}. In the limit of $P_{\mathrm{int}} \gg P_{\mathrm{ext}}$, we can calculate an asymmetry parameter for the energy-relaxation times in the shield up or down positions,

$$A_i = 2\frac{\Gamma_1^{\mathrm{d},i}-\Gamma_1^{\mathrm{u},i}}{\Gamma_1^{\mathrm{d},i}+\Gamma_1^{\mathrm{u},i}} \approx \frac{\eta^{\mathrm{u}}-\eta^{\mathrm{d}}}{2}\frac{P_{\mathrm{ext}}}{P_{\mathrm{int}}+\frac{\Gamma_{\mathrm{other}}}{a\sqrt{\omega_{\mathrm{q}}}}}, \tag{10}$$

where the index i refers to different rounds of the shield up/down experiment. The internal radiation rate P_{int} can be estimated using the experimentally measured median asymmetry parameter as

$$\tilde{P}_{\mathrm{int}} \approx \frac{(\eta^{\mathrm{u}}-\eta^{\mathrm{d}})}{2\langle A\rangle}P_{\mathrm{ext}} = 7.9\ \mathrm{keV\ mm^{-3}\ s^{-1}}, \tag{11}$$

where $\tilde{P}_{\mathrm{int}} = P_{\mathrm{int}} + \Gamma_{\mathrm{other}}/(a\sqrt{\omega_{\mathrm{q}}})$ and $\langle A\rangle \approx 0.0028$ (see Extended Data Fig. 8). This gives the upper bound for P_{int}. Owing to the other relaxation mechanisms, the actual value of P_{int} is lower. For example, $\Gamma_{\mathrm{other}} = 1/200\ \mu\mathrm{s}^{-1}$ would yield $P_{\mathrm{int}} \approx 1.6\ \mathrm{keV\ mm^{-3}\ s^{-1}}$ for the parameters of Q1. Here we emphasize that the estimate of the asymmetry parameter is based on the data gathered on all seven qubits used in the lead shield experiment, with all the qubits having different (fluctuating) values of Γ_{other}.

Efficiency of the lead shield

The reduction factor of external γ-radiation by the lead shield was evaluated using the radiation transport simulation described previously. In the simulation, γ-rays with energies drawn from the equilibrium emission spectra for ^{238}U, ^{232}Th and ^{40}K were generated isotropically from the surface of a sphere with 2.4 m diameter, centred on the qubits. The sphere completely enclosed the model for the lowered lead shield and the dilution refrigerator. The fraction of flux Φ reaching a smaller 17-cm-diameter sphere (fully inside the dilution refrigerator) was recorded. The table in Extended Data Fig. 6b shows the results for the no shield, shield down, and shield up, as well as the individual shield efficiency values $\eta^{\mathrm{u}} = 1-(\Phi^{\mathrm{u}}/\Phi^{\mathrm{noshield}})$ and $\eta^{\mathrm{d}} = 1-(\Phi^{\mathrm{d}}/\Phi^{\mathrm{noshield}})$.

A similar simulation was performed to calculate the efficiency of the lead shield against cosmic rays. As expected, the lead shield is ineffective at blocking cosmic rays, but works well against γ-rays originating from the nuclear decay events in the laboratory (see Extended Data Fig. 6c).

To validate the simulations, the NaI detector was operated separately inside the lead shield at the approximate location of the qubits in the shield-up configuration. This configuration was also simulated, and the output fitted to the measured spectrum using the same fit procedure as for the bare NaI. If the simulation and fit procedure are accurate, both fits should give the same values for the input flux. The results are reported in the first rows of the table in Extended Data Fig. 6b. The results for U and Th are consistent, whereas the values for K differ by about 2.5σ. It may be that the lead itself has a high level of ^{40}K, but we treat this as a systematic uncertainty, which is 7% of the total γ-ray flux.

Extended Data Fig. 1b–d shows a diagram of the lead shield and its dimensions.

Statistical analysis of the lead shield experiment

Since there are considerable fluctuations in the internal energy-relaxation rates Γ_{other} of the qubits, we performed a careful A/B test to verify that the effect of the lead shield on the qubit energy-relaxation time was not due to statistical error. In the measurement of the energy-relaxation rates of the qubits, there is uncertainty both due to the measurement accuracy and due to the fluctuations and drifts in the energy-relaxation rates over time. To reduce the uncertainty due to the measurement accuracy, we measured the energy-relaxation rates N times in each step of the A/B test. After N measurements the position of the lead shield was swapped (up versus down) and we performed another N measurements. This cycle was repeated 65 times with a sample containing qubits Q1 and Q2. To accelerate data acquisition, we installed a second sample with five qubits (Q3–Q7) and repeated the measurement cycle an additional 85 times. We used $N = 50$ for qubits Q1 and Q2, and $N = 10$ for qubits Q3–Q7 (see Extended Data Fig. 3a, c for the measured energy-relaxation rates). The median energy-relaxation times of the qubits are listed in the table in Extended Data Fig. 1e.

In the spirit of a Dicke radiometer experiment, performing repeated short measurement cycles was crucial for reducing the uncertainty in the relaxation rates due to drifts that occurred on timescales longer than the cycle period. The drift has been attributed in part to fluctuating two-level systems in dielectrics close to the qubit and in the junction region. However, by raising and lowering the shield often enough (every 50th measurement for qubits Q1 and Q2, and every 10th measurement for qubits Q3–Q7), the slow drift is mostly cancelled. Extended Data Fig. 3d shows the spectral density of the T_1 noise for qubits Q3, Q4, Q6 and Q7. The noise power density approximately follows a power law $S = \mathrm{const}/f^{\alpha}$ with $\alpha \approx 1.5$. The fit to the model is shown with a solid orange line. The noise power density at the lead shield up/down cycle frequency of $1/(15 \pm 1\ \mathrm{min})$ is $3.4 \times 10^4\ \mu\mathrm{s}^2\ \mathrm{Hz}^{-1}$. The noise power in the measurement can be estimated by integrating the spectral density over the noise bandwidth, which for the lock-in measurement yields $49\ \mu\mathrm{s}^2$ (shaded red area in Extended Data Fig. 3d). If all the data were gathered sequentially, the noise power can be estimated to be $718\ \mu\mathrm{s}^2$ (grey shaded are in Extended Data Fig. 3d), over an order of magnitude higher than in the Dicke experiment.

We used the median to estimate the net change $\delta\Gamma_1$ (between shield-up and shield-down configurations) to reduce sensitivity to individual measurement outliers. The quasiparticle contribution to the energy-relaxation rates of the qubits depends on their frequencies according to equation (5), and therefore we have normalized the changes in the energy-relaxation rates to the frequency of Q1 by multiplying by a conversion factor $\sqrt{\omega_{\mathrm{q}}^{(\mathrm{Q1})}/\omega_{\mathrm{q}}^{(\mathrm{Q}i)}}$.

We neglected a small percentage of the total data points where Γ_1^{u} or Γ_1^{d} was less than $1/30\ \mu\mathrm{s}^{-1}$ or their difference was more than 10 standard deviations of all the measured differences, as these tended to indicate suspect rates derived from poorly resolved decay functions. We then calculated the 95% CIs for $\delta\Gamma_1$ using the normal approximation for the CI of the sample median[46].

We applied the Wilcoxon signed-rank test to determine whether the median of the two distributions (corresponding to the shield-up versus shield-down configurations) differed in a statistically significant manner. This is a non-parametric test and can be used for data that are not normally distributed. For $\delta\Gamma_1$, the single-sided Wilcoxon signed-rank test gives a P-value of $P = 0.006$ for the null hypothesis that the median of the energy-relaxation rates with the shield is the same or higher than without the shield. The test statistic $w \approx 25{,}000{,}000$ with a sample size of 9,846. For $P \ll 0.05$, we can reject this null hypothesis and conclude that the shield reduces the energy-relaxation rate.

We performed several tests to verify the correctness of our statistical analysis. First, we checked that the result is not sensitive to the post-processing that we performed on the data. The first panel of Extended Data Fig. 7a shows the P-value of the Wilcoxon signed-rank test for a range of different cut-off parameters. The P-value remains low for all the realistic parameters we tested, verifying that the finding is not an artefact of post-processing or parameter selection. The median value is even less sensitive to the post-processing, shown in the

lower-left panel. The blue diamond in the upper-left corner shows the point where no post-processing is done. The blue circle shows the values that we use in the main text, $T_1^{\mathrm{cut-off}} = 30\ \mu\mathrm{s}$ and $n_\sigma^{\mathrm{cut-off}} = 10$.

Next, we tried shuffling the data by comparing the energy-relaxation rates of the measurements to the next measurement without moving the shield. In this case, we would expect the signal to vanish completely, and the null hypothesis to be manifestly true. The result is shown in the middle column of Extended Data Fig. 7a. In this case, the *P*-value is close to 1, which implies that we must accept the null hypothesis that there is no signal if we do not move the shield, as expected.

In the third test, we completely randomized the pairs of measurements that we compared, resulting in overall high *P*-value, supporting our analysis (third column).

Extended Data Fig. 7b shows a section of Extended Data Fig. 7a along the dashed lines in the left and middle panels. The shaded areas show the 68% CI of the medians.

Data availability

The data that support the findings of this study are available from the corresponding author upon reasonable request and with the permission of the US Government sponsors who funded the work.

Code availability

The code used for the analyses is available from the corresponding author upon reasonable request and with the permission of the US Government sponsors who funded the work.

41. Wallraff, A. et al. Approaching unit visibility for control of a superconducting qubit with dispersive readout. *Phys. Rev. Lett*. **95**, 060501 (2005).
42. Macklin, C. et al. A near–quantum-limited Josephson traveling-wave parametric amplifier. *Science* **350**, 307–310 (2015).
43. Yan, F. et al. The flux qubit revisited to enhance coherence and reproducibility. *Nat. Commun*. **7**, 12964 (2016).
44. Tanabashi, M. et al. Review of particle physics. *Phys. Rev. D* **98**, 030001 (2018).
45. Hagmann, C., Lange, D. & Wright, D. Cosmic-ray shower generator (CRY) for Monte Carlo transport codes. *IEEE Nucl. Sci. Symp. Conf. Rec*. **2**, 1143–1146 (2007).
46. Mangiafico, S. S. Summary and analysis of extension program evaluation in R (Rutgers Cooperative Extension, 2016).

Acknowledgements We thank K. Serniak and R. Winik for discussions and comments on the manuscript; G. Calusine, K. Serniak and U. von Luepke for designing and pre-characterizing the qubit samples; G. Castelazo for assistance with operating the lead shield; M. S. Galanek, R. Samz and A. Greene for assistance in oversight of radiation source use; M. R. Ames and T. I. Bork at the MIT Reactor (MITR) for production of the ^{64}Cu source; and M. A. Zalavadia for providing the NaI detector. This work was supported in part by the US Department of Energy Office of Nuclear Physics under an initiative in Quantum Information Science research (contract award no. DE-SC0019295, DUNS: 001425594); by the US Army Research Office (ARO) grant W911NF-14-1-0682; by the ARO Multidisciplinary Research Initiative W911NF-18-1-0218; by the National Science Foundation grant PHY-1720311; and by the Assistant Secretary of Defense for Research and Engineering via MIT Lincoln Laboratory under Air Force contract no. FA8721-05-C-0002. A.H.K. acknowledges support from the NSF Graduate Research Fellowship program. Pacific Northwest National Laboratory is operated by Battelle Memorial Institute under contract no. DE-AC05-76RL01830 for the US Department of Energy. We acknowledge IARPA and Lincoln Laboratory for providing the TWPA used in this experiment.

Author contributions This research project was a collaboration between experts in quantum systems (A.P.V., A.H.K., F.V., S.G. and W.D.O.) and nuclear physics (J.A.F., J.L.O., B.A.V., B.L. and A.S.D). Simulations of background radiation and the impact of the radiation shielding were performed by A.S.D., B.L., and J.L.O. D.K.K., A.J.M., B.M.N. and J.L.Y. fabricated the qubit chips. The qubit experiments and data analysis were performed by A.P.V., A.H.K. and F.V. All authors contributed to writing and editing of the Article. A.P.V. should be contacted on matters concerning qubit operations, and J.L.O. should be contacted on matters concerning radiation exposure.

Competing interests The authors declare no competing interests.

Additional information
Supplementary information is available for this paper at https://doi.org/10.1038/s41586-020-2619-8.
Correspondence and requests for materials should be addressed to A.P.V. or J.L.O.
Reprints and permissions information is available at http://www.nature.com/reprints.

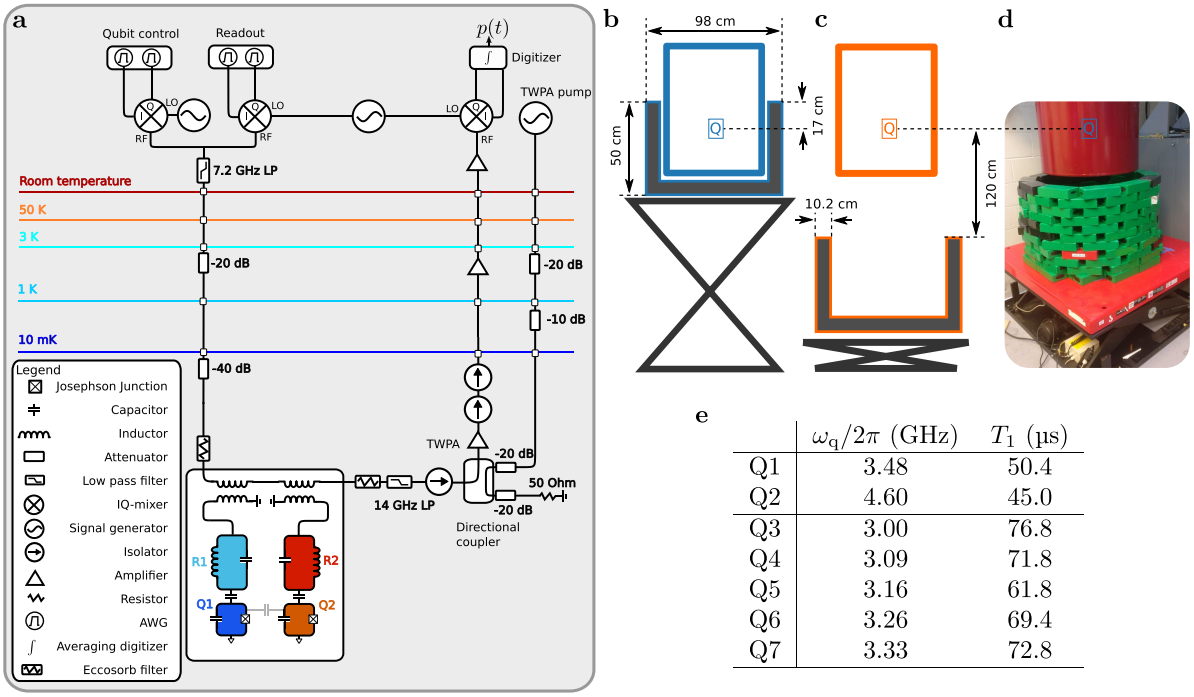

e

	$\omega_q/2\pi$ (GHz)	T_1 (μs)
Q1	3.48	50.4
Q2	4.60	45.0
Q3	3.00	76.8
Q4	3.09	71.8
Q5	3.16	61.8
Q6	3.26	69.4
Q7	3.33	72.8

Extended Data Fig. 1 | Experimental set-up. a, Simplified block diagram of the room-temperature electronics and dilution refrigerator configuration used for measuring the qubit frequency and coherence times. **b**–**d**, Schematic of the lead shield used to block environmental radiation. The lead shield can be raised and lowered by a scissor lift. **b**, In the up position, the qubits were 17 cm below the edge of the lead shield. **c**, In the lowered position, the edge of the lead shield was 120 cm below the qubits. **d**, Picture of a partially raised lead shield (in between the configurations shown in **b** and **c**). The lead bricks are wrapped in protective plastic film. **e**, The parameters of the qubits used in the lead shield experiment.

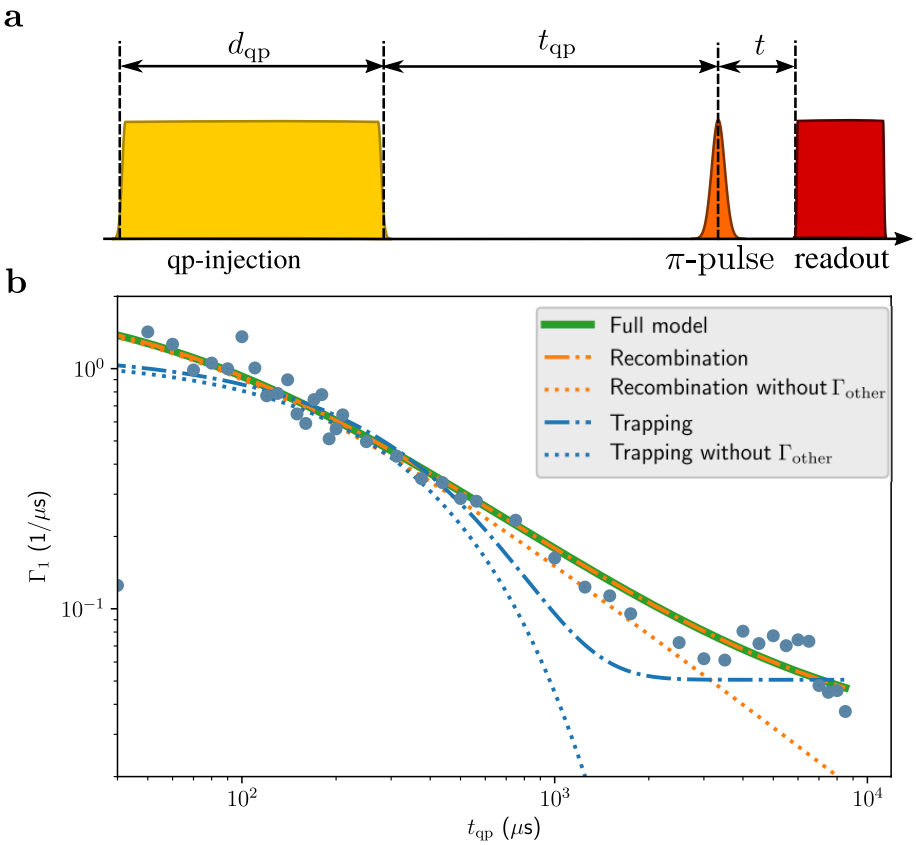

Extended Data Fig. 2 | Quasiparticle injection experiment. a, The pulse sequence in the quasiparticle injection experiment. First, a strong microwave pulse is applied for the duration of d_{qp} to the resonator, which excites quasiparticles. After time t_{qp}, the energy-relaxation time of the qubit is measured. **b**, The energy-relaxation rate of the qubit Q1 during the quasiparticle injection experiment (blue dots). A solid green line shows a fit to the data using the full model that includes quasiparticle trapping and recombination. Orange dash-dotted line shows the model with only recombination; dotted line shows the same model without the internal quasiparticle relaxation rate Γ_{other}. Blue dash-dotted line shows the fit to the model that only includes trapping of quasiparticles. Dotted blue line shows the trapping model without Γ_{other}.

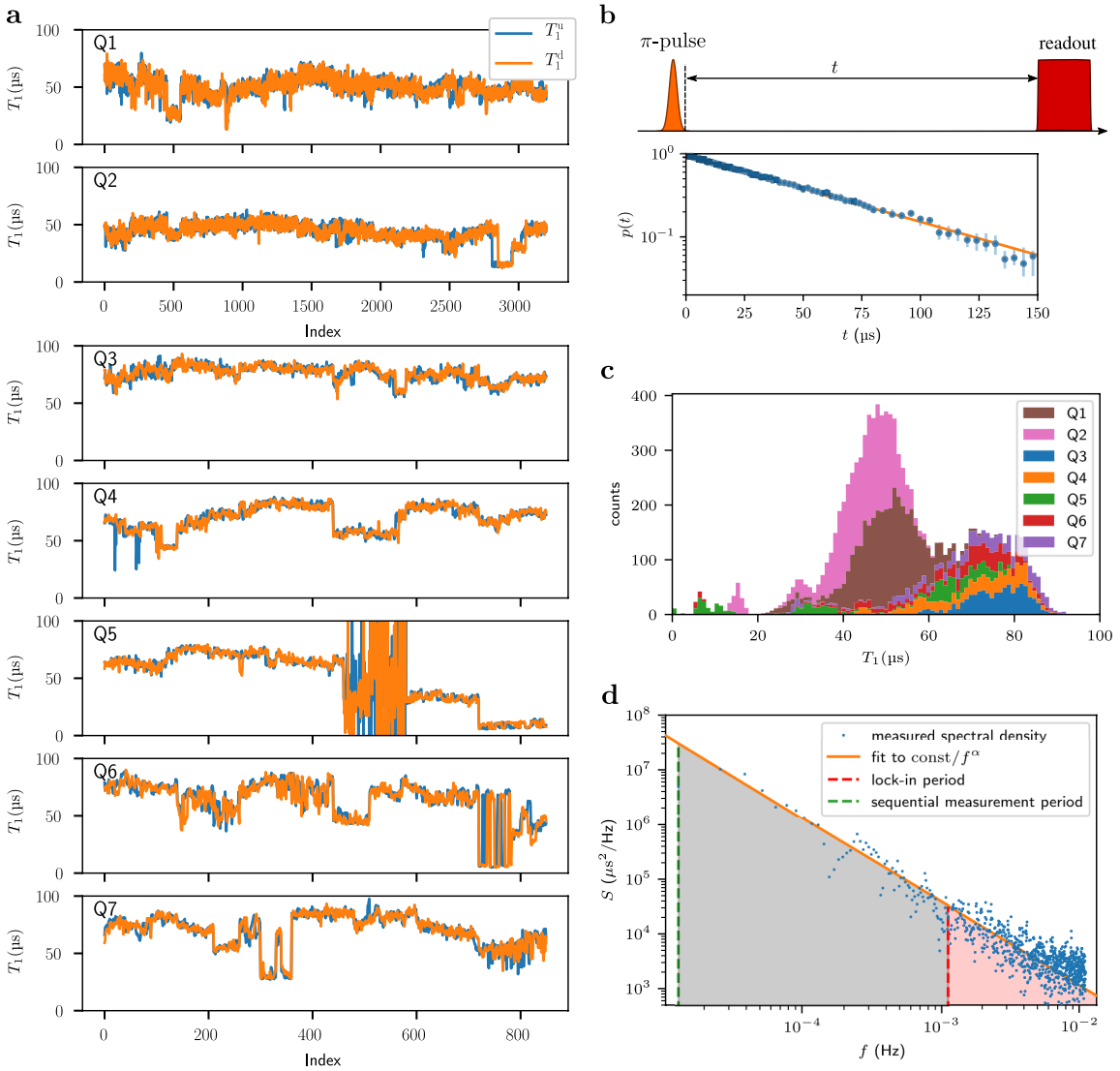

Extended Data Fig. 3 | Energy-relaxation times in the shielding experiment. **a**, Energy relaxation times T_1 for qubits Q1–Q7 during the lead shield experiment while the shield is in up (blue) or down (orange) positions. **b**, The pulse sequence used to measure the energy-relaxation rate of all the qubits. First, a π-pulse is applied to all the qubits. After time t, a measurement pulse is used to determine the state of the qubits. The qubit excited-state population relaxes exponentially as a function of time. Blue circles show the measured qubit excited-state populations, and the orange line is an exponential fit using the model of equation (2). **c**, Stacked histogram of the combined energy-relaxation times for all of the qubits in the lead shield experiment. **d**, Plot of the noise power spectral density during the lead shield experiment for qubits Q3, Q4, Q6 and Q7. The red dashed line marks the rate of a single cycle of the lead shield. The green dashed line shows the estimated measurement period if all the data were gathered sequentially. Orange line is a fit to a power law, $S = \text{const}/f^\alpha$, with $\alpha \approx 1.5$.

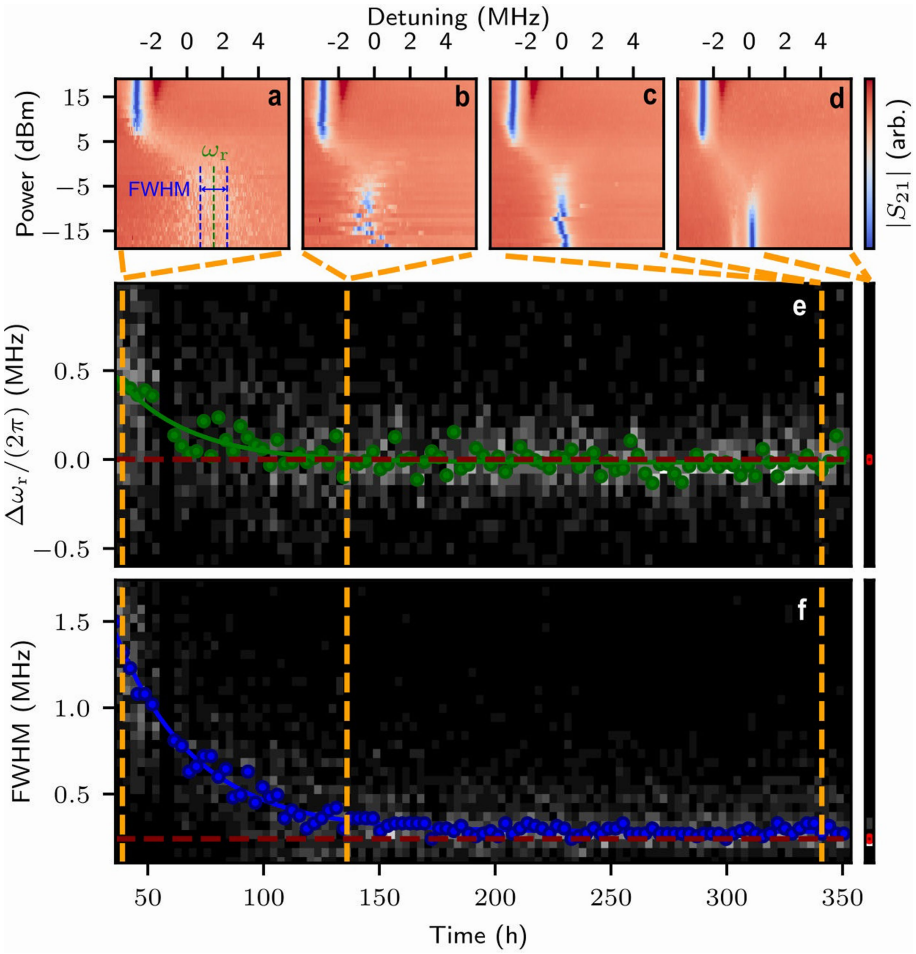

Extended Data Fig. 4 | Resonator single-tone spectroscopy. a–**d**, The transmission coefficient $|S_{21}|$ of resonator 1 as a function of readout power and readout frequency at different times throughout the experiment. When exposed to a high level of radiation, the resonator frequency becomes unstable in the dispersive regime that is used for reading out the qubit. The resonator becomes more stable as the radiation source decays. **e**, The change in the resonance frequency, $\Delta\omega_r$, due to radiation throughout the experiment. We observe that the median $\Delta\omega_r$ follows an exponential decay with a half-life of $t_{1/2} = 21.74 \pm 2.8$ h. **f**, Furthermore, the full-width at half-maximum (FWHM) of the resonator also exponentially decays with a half-life of $t_{1/2} = 24.16 \pm 0.78$ h until it converges to the control value.

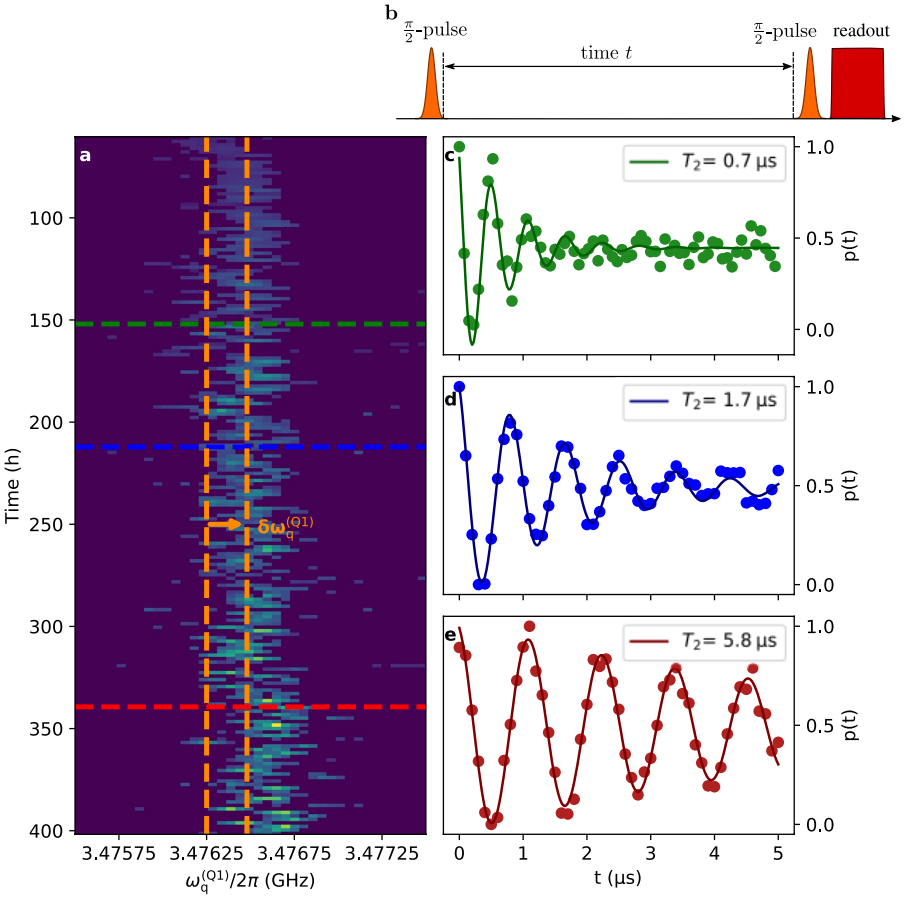

Extended Data Fig. 5 | Qubit frequency shift. a, The frequency of the qubit can be determined from a Fourier transform of a Ramsey measurement, shown at different times after installation of the ^{64}Cu source. We plot the inferred qubit frequency by offsetting the measured Fourier transform spectra by the frequency of the control pulses. The orange dashed lines show the shift in the average qubit frequency during the experiment. **b**, The pulse sequence used in a Ramsey measurement. The first π/2-pulse prepares the qubit in a superposition state. The phase of the qubit state evolves during time t, after which a second π/2-pulse is applied before the measurement pulse. **c**–**e**, Ramsey oscillations and fit T_2 times are shown at 152 h, 212 h and 340 h after installation of the ^{64}Cu source. The dashed lines in **a** show the times at which the measurements are performed.

a **Contaminants in the source**

Isotope	Half-life	nCi	± %
^{65}Zn	244 d	0.042	10%
^{75}Se	120 d	0.006	50%
^{110m}Ag	250 d	0.062	4%
^{122}Sb	2.724 d	0.022	32%
^{124}Sb	60 d	0.014	11%
^{198}Au	2.697 d	0.497	2%

b **Flux from nuclear decays**

Isotope	K	Th	U
Lab flux (cm^{-2}s^{-1})			
bare fit	2.8 ± 0.1	2.7 ± 0.6	1.3 ± 0.1
shielded fit	3.3 ± 0.2	2.7 ± 0.8	1.3 ± 0.02
difference	-0.5 ± 0.2	0.1 ± 1	-0.01 ± 0.2

Flux fraction reaching qubit

Isotope	K	Th	U
no shield	0.1232	0.1014	0.1003
shield down	0.1181	0.0978	0.0968
shield up	0.0284	0.0214	0.0208
η^{d}	0.041	0.036	0.035
η^{u}	0.769	0.789	0.793

c **Average shield efficiency**

	η^{d}	η^{u}
external gammas	0.038 ± 0.007	0.781 ± 0.002
cosmic rays	–	0.02 ± 0.02
Total	0.022 ± 0.003	0.461 ± 0.001

d **Absorbed power density in the sample**

	Al	Si
ρ_{src} (keV mm^{-3}s^{-1}µCi^{-1})	8.8	3.3
P_{ext} (keV mm^{-3}s^{-1})	0.1	0.094

e

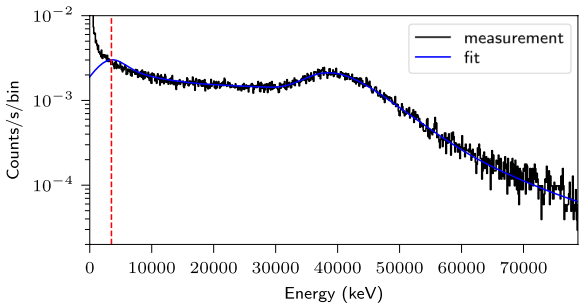

Extended Data Fig. 6 | Radiation transport simulations. a, Isotopes measured to be present in the reference sample (A-Ref) and their activities inferred for sample A as of 24 May 2019 at 4:00 p.m. Eastern time zone. **b**, Results from simulations of environmental radiation sources in the laboratory environment. The background γ-ray flux is obtained by a fit to a measurement with a NaI scintillator (Fig. 3a), simulating and measuring both with and without the lead shield in the 'up' position. Cosmic rays were also measured and simulated for both shield-up and shield-down conditions; the shield did not have a measurable effect in the up position, as expected, and the effect is taken to be zero in the down position. **c**, The average shield effectiveness values η are weighted by each component's contribution to total external power. Statistical uncertainties on the fraction of flux reaching the interior of the dilution refrigerator are all 0.0001; uncertainties on η-values for individual isotopes are all approximately 0.001. **d**, Power densities absorbed in silicon and aluminium. **e**, The figure shows the spectrum of the energy deposited in a NaI detector by cosmic-ray muon secondaries measured in the laboratory. The blue solid line shows the known cosmic-ray muon spectrum fit to the measured data. The spectrum corresponding to energies below the dashed red line is shown in Fig. 3a. Note that in the spectrum shown here, a different energy bin width is used to capture higher energy scales.

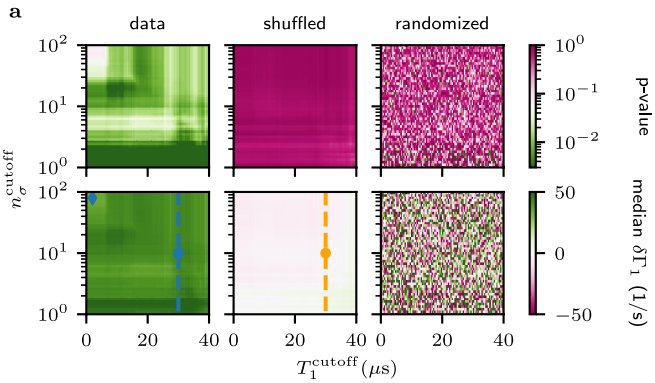

Extended Data Fig. 7 | The effect of post-processing on the lead shield effect A/B test. a, The upper row shows the *P*-value of the Wilcoxon signed rank test for three different test cases and for the different post-processing parameters. On the horizontal axis, the $T_1^{\mathrm{cut-off}}$ is varied. The vertical axis shows the effect of applying a cut-off to the difference in the energy-relaxation rates when the shield status is changed. The first column shows the actual data. The middle column shows a reference experiment, in which the energy-relaxation rates are compared without moving the shield. The last column shows the data when the energy-relaxation rate pairs are randomized. The lower row shows the median of the effect of the shield on the energy-relaxation rate $\delta\Gamma_1$. **b**, The median of $\delta\Gamma_1$ along the dashed lines in **a**. The shaded area shows 68% CIs for the median.

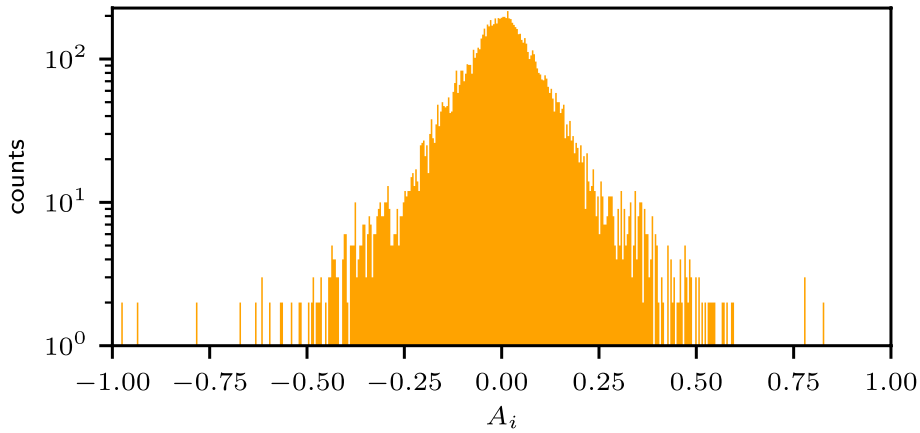

Extended Data Fig. 8 | Asymmetry parameter distribution. The distribution of the asymmetry parameter A_i of the energy-relaxation rates between the shield in up or down position.